Pore scale modeling of drainage displacement patterns in association with geological sequestration of CO_2

Ioannis Zacharoudiou[1], Edo S. Boek[2], and John Crawshaw[1]

[1]Qatar Carbonates and Carbon Storage Research Centre, Department of Chemical Engineering, Imperial College London, South Kensington Campus, London SW7 2AZ, United Kingdom

[2]School of Engineering and Materials Science, Queen Mary University of London, Mile End Road, London E1 4NS, United Kingdom

Key Points:

- Inertial effects cannot be neglected in the range of typical average capillary numbers (Ca_{av}) associated with multiphase flow in permeable media ($Ca_{av} \leq 10^{-3}$).
- Even as the average capillary (Ca_{av}) and Reynolds (Re_{av}) numbers decrease away from the injection point, inertial effects become important during abrupt jump events (Haines jumps).
- The local Ca_l and Re_l during jump events is orders of magnitude higher than the average flow dimensionless numbers.
- The maximum local Reynolds number Re_l during jumps is of the order 10^1.
- The Ohnesorge number, which reflects the thermophysical properties of the system under investigation, links the capillary and Reynolds numbers and should be used to restrict the parameter selection process.
- A Navier-Stokes solver should be used to investigate pore scale displacement processes.

Corresponding author: Ioannis Zacharoudiou, i.zacharoudiou@imperial.ac.uk

Abstract

We investigate the immiscible displacement (drainage) of a wetting fluid in a porous medium by a non-wetting fluid using multi-GPU lattice Boltzmann simulations with the aim of better understanding the pore scale processes involved in the geological sequestration of CO_2. Correctly resolving the dynamics involved in multiphase flow in permeable media is of paramount importance for any numerical scheme. Generally the average fluid flow is assumed to be at low Reynolds numbers Re_{av}. Hence, by neglecting inertial effects, this immiscible displacement should be characterised by just two dimensionless numbers, namely the capillary number Ca_{av} and the viscosity ratio, which quantify the ratio of the relevant forces, i.e. the viscous and capillary forces. Our investigation reveals that inertial effects cannot be neglected in the range of typical capillary numbers associated with multiphase flow in permeable media. Even as the average Ca_{av} and Re_{av} decrease away from the injection point, inertial effects remain important over a transient amount of time during abrupt Haines jumps, when the non-wetting phase passes from a narrow restriction to a wider pore space. The local Re_l at the jump sites is orders of magnitude higher than the average Re_{av}, with the local dynamics being decoupled from the externally imposed flow rate. Therefore, a full Navier-Stokes solver should be used for investigating pore scale displacement processes. Using the Ohnesorge number to restrict the parameter selection process is essential, as this dimensionless number links Ca_{av} and Re_{av} and reflects the thermophysical properties of a given system under investigation.

1 Introduction

The immiscible displacement of a fluid in a porous medium is of extreme importance in a plethora of applications, including hydrocarbon recovery, geological sequestration of CO_2 in saline aquifers etc. This has prompted experimental and numerical investigations of these phenomena, as understanding the factors affecting the displacement patterns becomes of paramount importance. Lenormand et al. (1988) investigated numerically and experimentally the immiscible displacement of a wetting (w) fluid in a micromodel by a non-wetting (nw) fluid. Completely neglecting inertial effects and considering only viscous and capillary forces, the drainage displacement process is governed by the ratio of these forces. Hence, Lenormand et al. (1988) argue that this can be characterized by: a) the ratio of viscous forces in both fluids, quantified by the ratio of the

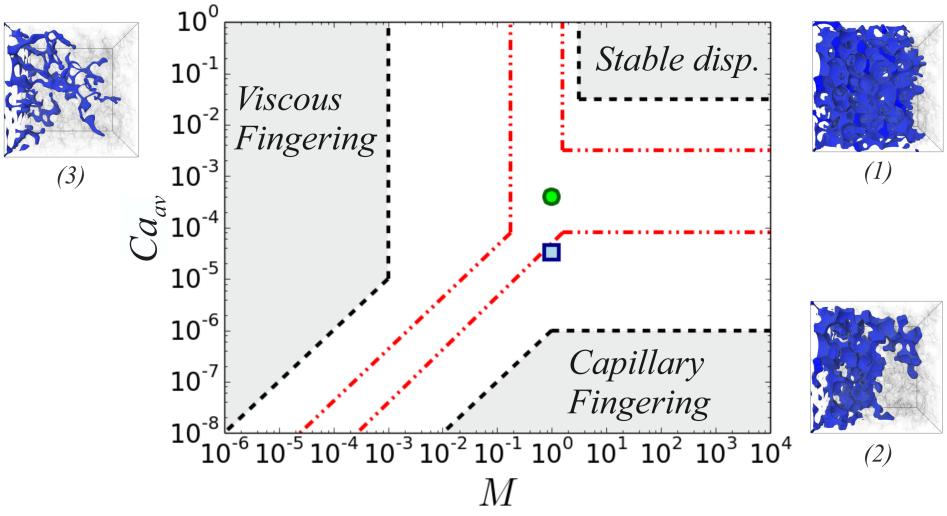

Figure 1. Lenormand's phase diagram for drainage and the domains of validity for the three displacement patterns: (1) stable displacement, (2) capillary and (3) viscous fingering. The gray zones denote the domains indicated by the simulations of Lenormand et al. (1988), while the boundaries given by the dashed dotted lines are from the experimental work of Zhang et al. (2011). These boundaries are shown here just for qualitative purposes, as they are strongly dependent upon the geometry type. The three configurations shown for illustration purposes of the three typical displacement patterns are from drainage simulations in Ketton limestone (see Fig. 2). The injected non-wetting phase is shown in blue, while rock grains and wetting phase are transparent. The two points correspond to the test cases examined in section 3.1.

dynamical viscosities η_i $(i = \mathrm{w}, \mathrm{nw})$, $M = \eta_{\mathrm{nw}}/\eta_{\mathrm{w}}$, and b) the ratio of viscous forces which act in the injected fluid over capillary forces. This is given by the average capillary number $Ca_{av} = \eta_{\mathrm{nw}}\bar{u}/\gamma$, where $\bar{u}$ and γ are the average velocity of the injected fluid and interfacial tension respectively. Of course the fluids' affinity to the porous media (i.e. wettability) should have a profound influence on the displacement patterns (Zhao et al., 2016; Singh et al., 2017; Rabbani et al., 2017). Depending on the dimensionless numbers above, either viscous or capillary forces dominate and the displacement pattern takes one of the basic forms: (a) viscous fingering, (b) capillary fingering or (c) stable displacement. The domains of validity of the different basic mechanisms can be mapped onto the (Ca_{av}, M) phase plane, which has been called the "phase-diagram" for immiscible displacements (Lenormand et al., 1988), see Fig. 1.

At high values of the capillary number and viscosity ratios the stable displacement regime is observed, where the principal force is due to the viscous forces in the injected fluid. Capillary effects and pressure drop in the displaced fluid are negligible. At values of the viscosity ratio below 1, i.e. when the injected fluid has lower viscosity than the viscosity of the wetting fluid, and at high values of the capillary number, then the viscous fingering instability dictates the displacement pattern. Here the principal force is due to the viscous forces in the displaced fluid, with capillary effects and pressure drop in the displacing fluid being negligible. Viscous fingers formed grow towards the mean direction of the flow. Finally the third regime, observed at low values of the capillary number, is called the capillary fingering regime. Viscous forces are negligible and the principal force is due to capillary forces. The fingering process is distinctively different to the one observed in the viscous fingering regime as now fingers form loops and grow in all directions. The boundaries between the different displacement pattern regimes depend on the details of the geometry used and the degree of fluid wettability on solid surfaces.

Yortsos et al. (1997) also provide a phase diagram of fully developed drainage in porous media with axes the viscosity ratio and capillary number and postulate a description in terms of invasion percolation in a gradient. They recognize the existence of two different global patterns, depending on whether invasion is in a stabilizing gradient or a destabilizing gradient, respectively, and propose that the various properties of the flow regimes can be deternined by the spatial variation of the percolation probability and the sign of its gradient.

The important question to be addressed is whether we should indeed neglect completely inertial effects, when it comes to modeling two phase flow at the pore scale, for example for CO_2 geological sequestration or hydrocarbon recovery. Furthermore, what conditions, flow regimes, or systems of fluids would justify this choice and render Ca_{av} and M sufficient to fully capture the physics of fluid displacement. Lenormand's phase diagram (Lenormand et al., 1988) provides a qualitative picture about the overall drainage displacement patterns. However, when it comes to quantifying important aspects of two-phase flow, for example: a. the fluids' spatial distribution/connectedness, b. the displacement efficiency (limiting value for the injected phase saturation) in the different flow regimes or c. the flow regimes' domain boundaries, we need to question whether the above treatment is sufficient. In terms of direct numerical modeling this is of paramount importance,

as it affects the setup of the simulations and the parameter selection process; this consequently determines the reliability of the numerical results and their predictive capabilities.

When considering processes like hydrocarbon recovery (brine displacing oil) or CO_2 geological sequestration (CO_2 displacing brine), generally, the average fluid flow at the pore scale is assumed to be at low Reynolds numbers; especially, as the distance from the injection point in the well bore increases. However, considerable work in the literature demonstrates the relevance of inertial effects in multiphase flow during both imbibition (Ferrari & Lunati, 2014; Zacharoudiou et al., 2017) and drainage (Moebius & Or, 2014; Kazemifar et al., 2016; Li et al., 2017). During imbibition, interfacial oscillations and inertia can affect the displacement sequence/pathways (Ferrari & Lunati, 2014) and hence the displacement efficiency. Capillary filling dynamics is also not fully captured by just the capillary number, as the choice of parameters affects the dissipation of energy in the system, leading to different dynamics, e.g. wetting film propagation (Zacharoudiou et al., 2017).

In a drainage situation, inertial effects can be also important over a transient amount of time, during Haines jump events (Berg et al., 2013; Armstrong & Berg, 2013; Armstrong et al., 2015; Zacharoudiou et al., 2018). During these sharp interfacial jumps, capillary forces accelerate the fluid interface, as it passes from a narrow restriction to a wider pore body, while initially inertial and viscous forces oppose the motion. This leads locally to fluid velocities that can be orders of magnitude higher than the average fluid velocity. Kazemifar et al. (2016) and Li et al. (2017) report maximum local Reynolds numbers in the range of 10^2 and 10^1 in supercritical CO_2 - water experiments in 2D homogeneous and heterogeneous porous micromodels respectively, exceeding the range of validity of Darcy's law. At a second stage, as the interface decelerates, inertial and capillary forces become the driving forces, opposed by viscous forces; the time scales of this stage constitute the majority of the pore draining times (Zacharoudiou & Boek, 2016). As inertia becomes a driving force, it can affect the invasion of subsequent throats. The numerical work of Moebius and Or (2014) on drainage in a 2D pore-throat network, revealed the role of inertia in shifting the distribution of invaded throats by including smaller invaded throats compared to invasion patterns without inertia. This confirmed previous observations (Moebius & Or, 2012) that inertia affects local displacement patterns.

Another important feature of these abrupt events is the extensive fluid rearrangement taking place in the region of the jump, which contributes significantly to the draining of the pore body (Berg et al., 2013; Zacharoudiou et al., 2018). Experimentally, it has been observed that the draining of pore bodies occurs at time scales smaller than the time scales expected considering the externally imposed injection flow rate, indicating that cooperative filling dynamics takes place (Berg et al., 2013). We have confirmed this observation numerically using free energy lattice Boltzmann simulations on Ketton limestone (Zacharoudiou et al., 2018). Hence, we expect that completely neglecting inertial effects, which is a key element of the jumps, will not enable capturing the fluid flow dynamics and the associated features of these abrupt events, e.g. pressure drop, fluid rearrangement etc.

Therefore, it would be reasonable to question whether the description in terms of just the average capillary number Ca_{av} and the viscosity ratio M is sufficient to describe pore-scale two-phase flow behaviour correctly. In particular we question the usual approach in numerical simulations of keeping both Ca_{av} and Re_{av} low. The questions that need to be addressed, mainly from the modeling point of view, are the following:

- How small is the average flow Reynolds number $Re_{av} = \rho \bar{u} L_s / \eta_{\text{nw}}$ (L_s being the characteristic length scale of the system)?
- When does the transition from smooth flow to burst flow (Haines jumps) take place?
- What is the local Reynolds number Re_l due to interfacial instabilities, e.g. Haines jumps?

Although a significant amount of research deals with the numerical modeling of two phase flow at the pore scale (Raeini et al., 2014; Tsuji et al., 2016; Yamabe et al., 2015), a discussion on the parameter selection process is in most cases lacking. In our previous work in micromodels (Zacharoudiou & Boek, 2016; Zacharoudiou et al., 2017) we highlighted the need to numerically match not only the capillary number and the viscosity ratio, but also the Ohnesorge number for a given experimental system. Y. Chen et al. (2018) follow our approach for the parameter selection process in their lattice Boltzmann simulations in 2D heterogeneous micromodels and present a rigorous discussion on the matter. Here we extend our previous investigations to three dimensional permeable media. The paper is organized as follows. In the next section we provide the details of the numerical scheme we shall use. We present and discuss our results in section 3. We fo-

cus on demonstrating that Ca_{av}, M are not sufficient to fully describe two phase flow at the pore scale by examining simulations at fixed Ca_{av}, M and wettability conditions. We examine two cases at intermediate and low Ca_{av} (indicated in Fig. 1), with the latter being characterised by Haines jumps. The flow regimes examined (intermediate $Ca_{av} \sim 3 \times 10^{-4}$, low $Ca_{av} \sim 4 \times 10^{-5}$) can be considered sufficient for the purposes of the current investigation, given that we encounter the transition to the capillary fingering regime characterised by Haines jumps, expected at the low Ca_{av} flow. Typical values for the ratio of viscous to capillary forces at the pore scale, i.e. Ca_{av}, are in the range of 10^{-10}–10^{-3}, depending on the distance from the injection point in the well bore (Blunt & Scher, 1995). Then we examine individual jump events at varying Ca_{av}, demonstrating that the local Ca_l, Re_l are orders of magnitude higher than the corresponding average values. The local dynamics become decoupled from the externally imposed flow rate, as energy stored in the system during slow drainage as surface energy is released, driving these abrupt events and the corresponding fluid redistribution. Finally conclusions drawn from this work are discussed in section 4.

2 Numerical Model

In this section we describe the numerical method we shall use, starting with the thermodynamics in section 2.1, the dynamical equations of motion in section 2.2 and the lattice Boltzmann implementation in section 2.3.

2.1 Thermodynamics of the fluid

We consider a binary fluid mixture containing two types of molecules, A and B. The equilibrium properties of the binary fluid can be described by a Landau free energy functional (Briant & Yeomans, 2004), in terms of an order parameter ϕ,

$$\mathcal{F} = \int_V \left(f_b + \frac{\kappa_\phi}{2} (\partial_\alpha \phi)^2 \right) dV + \int_S f_s \, dS \, . \tag{1}$$

The order parameter is a scalar field, which describes the local molecular composition of the binary fluid mixture, defined as $\phi = (n_A - n_B)/(n_A + n_B)$. $n_{A,B}$ denotes the number density of the A, B molecules locally. For temperatures below a critical temperature T_c ($T < T_c$), the mixture undergoes phase separation into A-rich and B-rich domains, with the equilibrium values for the order parameter being $\phi_{eq} = \pm 1$. The first

term in the integrand is the bulk free energy density given by

$$f_b = \frac{a}{2}\phi^2 + \frac{b}{2}\phi^4 + \frac{c^2}{3}\rho \ln \rho \ , \tag{2}$$

where ρ is the fluid mass density and c is a lattice velocity parameter. This choice of f_b allows binary phase separation into two phases, if $a < 0$ and $b > 0$, with bulk equilibrium solutions $\phi_{eq} = \pm(-a/b)^{1/2}$. Making the choice $a = -b$, leads to $\phi_{eq} = \pm 1$ for the bulk of the two phases. The position of the fluid-fluid interface is chosen to be the locus $\phi = 0$. The term in ρ does not affect the phase behavior and controls the compressibility of the fluid (Kendon et al., 2001).

The energetic cost of fluid-fluid interfaces is accounted for by the gradient term $(\kappa_\phi/2)(\partial_\alpha \phi)^2$, which penalises spatial variations of the order parameter ϕ by a factor κ_ϕ, for example across the fluid-fluid interface. Taking the functional derivative of the free energy with respect to ϕ gives the exchange chemical potential

$$\mu \equiv \frac{\delta \mathcal{F}}{\delta \phi} = a\phi + b\phi^3 - \kappa_\phi \partial_{\gamma\gamma}\phi \ , \tag{3}$$

which is constant at equilibrium (set $\mu = 0$), otherwise it would give rise to a thermodynamic force density $-\phi\partial_\alpha \mu$. Assuming for simplicity that the fluid-fluid interface is flat and located at $x = 0$, eq. 3 alows an interface solution of the form $\phi(x) = \tanh(x/(\sqrt{2}\xi))$, with $\xi = \sqrt{-\kappa_\phi/a}$ being the interface width (Briant & Yeomans, 2004). Throughout this work we fix $\xi = 0.81$; this was previously shown to give accurate results for the variation of ϕ across the fluid-fluid interface (Kendon et al., 2001) and allows a smooth transition between the two phases over a length scale of $\sim 5\xi$. The corresponding interfacial tension (excess free energy per unit area) is given by $\gamma = \sqrt{-8\kappa_\phi a^3/(9b^2)}$ (Briant & Yeomans, 2004).

The choice of free energy functional leads to a pressure tensor (Anderson et al., 1998)

$$\begin{aligned} P_{\alpha\beta} &= \Big[\phi\frac{\delta \mathcal{F}}{\delta \phi} + \rho\frac{\delta \mathcal{F}}{\delta \rho} - \mathcal{F}\Big]\delta_{\alpha\beta} + (\partial_\alpha \phi)\frac{\delta \mathcal{F}}{\delta(\partial_\beta \phi)} \\ &= \Big[\mathrm{p}_b - \kappa_\phi \phi \partial_{\gamma\gamma}\phi - \tfrac{\kappa_\phi}{2}(\partial_\gamma \phi)^2\Big]\delta_{\alpha\beta} + \kappa_\phi(\partial_\alpha \phi)(\partial_\beta \phi) \\ &= \mathrm{P}^{iso}\delta_{\alpha\beta} + P^{chem}_{\alpha\beta} \ , \end{aligned} \tag{4}$$

where $p_b = \frac{c^2}{3}\rho + \frac{1}{2}a\phi^2 + \frac{3}{4}b\phi^4$ is the bulk pressure. $P_{\alpha\beta}$ consists of two terms: an isotropic contribution $P^{iso} = c^2 3\rho$ to ensure constant density and a 'chemical' pressure tensor contribution $P^{chem}_{\alpha\beta}$ (Kendon et al., 2001). The thermodynamics of the fluid is contained

in the later. It reflects the fact that in the presence of chemical potential gradients, a force density proportional to this will drive the system to equilibrium. This thermodynamic force density, $-\phi(\partial_\alpha \mu)$, can be expressed as the divergence of a 'chemical' pressure tensor $\phi(\partial_\alpha \mu) = \partial_\beta P^{chem}_{\alpha\beta}$.

The final term in the free energy functional, eq. 1, describes the interactions between the fluid and the solid surface. Following (Cahn, 1977), the surface energy density is taken to be of the form $f_s = -h\phi_s$, where ϕ_s is the value of the order parameter at the surface. Minimisation of the free energy gives an equilibrium wetting boundary condition (Briant & Yeomans, 2004)

$$\kappa_\phi \, \partial_\perp \phi = \frac{df_s}{d\phi_s} = -h \; . \tag{5}$$

The value of the parameter h (the surface excess chemical potential) is related to the equilibrium contact angle θ^{eq} via (Briant & Yeomans, 2004)

$$h = \sqrt{2\kappa_\phi b}\, \mathrm{sign}\left[\frac{\pi}{2} - \theta^{\mathrm{eq}}\right] \sqrt{\cos\left(\frac{\alpha}{3}\right)\left\{1 - \cos\left(\frac{\alpha}{3}\right)\right\}} \; , \tag{6}$$

where $\alpha = \arccos\left(\sin^2\theta^{eq}\right)$ and the function sign returns the sign of its argument.

2.2 Equations of motion

The hydrodynamic equations for the system are the continuity, eq. 7, and the Navier-Stokes, eq. 8, equations for a nonideal fluid

$$\partial_t \rho + \partial_\alpha(\rho u_\alpha) = 0 \; , \tag{7}$$

$$\partial_t(\rho u_\alpha) + \partial_\beta(\rho u_\alpha u_\beta) = -\partial_\beta P_{\alpha\beta} + \partial_\beta\left[\eta\left(\partial_\beta u_\alpha + \partial_\alpha u_\beta\right)\right] \; , \tag{8}$$

where $\mathbf{u}$, $\mathbf{P}$, η are the fluid velocity, pressure tensor and dynamic viscosity respectively. For a binary fluid the equations of motion are coupled with a convection-diffusion equation,

$$\partial_t \phi + \partial_\alpha(\phi u_\alpha) = M_\phi \nabla^2 \mu \; , \tag{9}$$

that describes the dynamics of the order parameter ϕ. M_ϕ is a mobility coefficient (see Appendix A, eq. Appendix A).

2.3 Lattice Boltzmann method

The numerical algorithm we use to solve the equations of motion is based on the lattice Boltzmann method (Doolen, 1990; Benzi et al., 1992; S. Chen et al., 1992; Succi,

2001). In particular, we use an extension of the method, the free energy LB method, first introduced by Swift et *al.* (Swift et al., 1995, 1996), to simulate two-phase flow. This algorithm belongs to a class of hydrodynamic models, called diffuse interface models (Jacqmin, 2000; Pierre & Seppecher, 1996; Briant et al., 2004; Briant & Yeomans, 2004), where the fluid-fluid interface has a finite size. Far away from a contact line, the method solves the hydrodynamic equations of motion of the fluid, i.e. the Navier-Stokes equations and the continuity equation. In the vicinity of the contact line, however, due to the finite size of the interface, the method introduces a diffusive mechanism, which regularizes the viscous dissipation singularity (de Gennes, 1985) and allows the contact line to slip on a solid substrate.

The above equations are solved using a Multiple Relaxation Time (MRT) lattice Boltzmann algorithm (D'Humières et al., 2002). Details of the implementation of the lattice Boltzmann algorithm are given in Appendix A. We note here that the numerical code implementation is performed in CUDA C++ to take advantage of accelerated computing on multiple general-purpose graphics processing units (GPGPUs).

3 Results

3.1 Drainage simulations at fixed Ca_{av} and M

We examine here whether the classical treatment of characterizing two-phase flow (drainage) at the pore scale in terms of just the capillary number $Ca_{av} = \eta_{\mathrm{nw}}\bar{u}/\gamma$, viscosity ratio $M = \eta_{\mathrm{nw}}/\eta_{\mathrm{w}}$ and wetting boundary conditions (θ^{eq}) (Lenormand et al., 1988) is sufficient to describe two phase flow. To this end we directly solve the hydrodynamic equations of motion in a three dimensional geometry reconstructed from micro-CT images of Ketton limestone (Shah et al., 2016) and consider fluid flows at fixed average capillary number Ca_{av} and viscosity ratio ($\log M = 0$). We note here that $\bar{u}$ is the average nw phase velocity, obtained from the simulations and not the one obtained from the injection flow rate. The simulation system size is 700^3 lattice units (l.u) at a resolution of 4.52 μm per l.u. (physical system size (3.16 mm)^3). The fluid flow is driven by applying a constant injection flow rate, which is achieved by applying velocity boundary conditions at the inlet/outlet of the simulation domain (Hecht & Harting, 2010). Small reservoirs are placed at the inlet/outlet of the simulation domain. The equilibrium con-

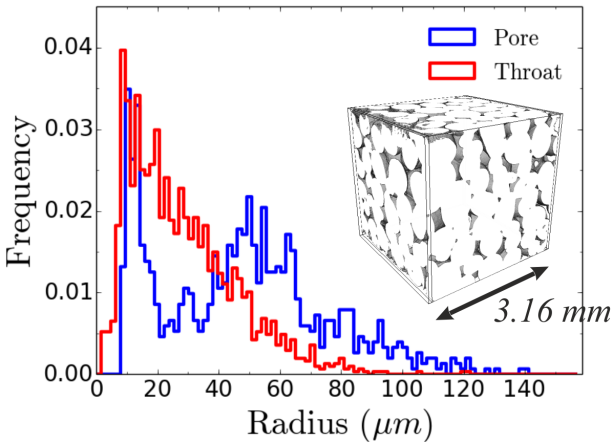

Figure 2. The pore and throat size distribution (Dong & Blunt, 2009) of the geometry used in the simulations (see inset). Inset: Ketton rock sample reconstructed from micro-CT images(Shah et al., 2017). The simulation system size is 700^3 lattice units (l.u) at a resolution of 4.52 μm per l.u, which corresponds to a physical system size of (3.16 mm)^3 with porosity 0.159. A small reservoir (16 l.u) is added at the inlet/outlet of the simulation domain.

tact angle is set to $\theta^{eq} = 40°$, consistent with contact angle measurements in Ketton at reservoir conditions for a supercritical CO_2 - brine system (Andrew et al., 2014).

3.1.1 Intermediate Ca_{av}

For the case of intermediate capillary number (indicated in Fig. 1 with the green circle), we consider three simulations with different volumetric injection flow rates, $Q_{inj} = \int_A \mathbf{u}_{inj} \cdot d\mathbf{A}$, and fluid viscosities, while maintaining the same average capillary number ($Ca_{av} = 3.3 \times 10^{-4}$) and viscosity ratio ($\log M = 0$). $\mathbf{A}$ is the cross sectional area at the inlet/outlet. Fixing Ca_{av} is achieved by keeping the product $Q_{inj}\eta_{\rm nw}$ and all other parameters (θ^{eq}, γ) constant. Simulation parameters (in lattice units - l.u) are listed in Table 1. The above choice essentially varies the Reynolds number ($Re_{av}^{(1)} = 1.0 \times 10^0$, $Re_{av}^{(2)} = 1.0 \times 10^{-2}$, $Re_{av}^{(3)} = 1.7 \times 10^{-3}$). Here we use the average invaded throat diameter as the characteristic length scale L_s in the definition of $Re_{av} = \rho \bar{u} L_s / \eta_{\rm nw}$, as this controls the pressure at which pores drain, $L_s \sim 10$ l.u ($45\mu m$). A useful dimensionless number that relates the capillary to Reynolds numbers is the Ohnesorge number

$$Oh^2 = Ca_{av}/Re_{av} = \eta_{\rm nw}^2/\rho\gamma L_s \ , \tag{10}$$

Table 1. Simulation parameters in lattice units - Intermediate Ca_{av} test case*

Run	η_{nw}	u_{inj}
1	1.67×10^{-1} ($\tau^{(1)}_{f,\mathrm{nw}} = 1.0$)	2×10^{-6}
2	6.67×10^{-2} ($\tau^{(2)}_{f,\mathrm{nw}} = 0.7$)	5×10^{-6}
3	6.67×10^{-3} ($\tau^{(3)}_{f,\mathrm{nw}} = 0.52$)	5×10^{-5}

*Simulations with fixed interfacial tension $\gamma = 1.17 \times 10^{-2}$ ($\kappa_\phi = 10^{-2}$, $a = -1.54 \times 10^{-2}$) and $\theta^{eq} = 40^\circ$.

which describes the relative importance of viscous forces to inertial and interfacial tension forces. As we will show by the end of this section, Oh will prove useful in restricting the parameter selection process in terms of numerical modeling.

We start by examining how the injected non-wetting fluid saturates/fills the porous rock. Fig. 3(a) shows the non-wetting phase saturation S_{nw} as a function of the frontal position, which is defined as the distance of the most deeply penetrated non-wetting phase from the inlet, see Fig. 3(c). Although there is a significant degree of overlap, it is clear that results are not completely the same. More importantly, different non-wetting phase saturation is obtained at breakthrough $S^{(br)}_{nw}$ (frontal position $l = 700$). Given the overlap of the results, we further examine configurations with the same S_{nw} and frontal position, aiming at inspecting the fluids' topology in the pore space. Fig. 3(b) shows the non-wetting phase saturation at planes perpendicular to the mean direction of the flow S^{yz}_{nw} as a function of the injection depth (distance of the yz-plane from the inlet), when the total saturation $S_{nw} = 0.3975$ and the frontal position is $l = 612$ (indicated with the red arrow in Fig. 3(a)). This clearly reveals that the above simulations actually exhibit a different spatial distribution of the fluids, which means that the displacement pathways/sequence might be different. A comparison of the fluids' spatial distribution for the simulations with the smallest $Re_{av} = 1.7 \times 10^{-3}, 1.0 \times 10^{-2}$ is shown in Fig. 3(d); regions in light blue and red denote the regions occupied by the non-wetting phase only for the case $Re_{av} = 1.0 \times 10^{-2}$ and $Re_{av} = 1.7 \times 10^{-3}$ respectively, while regions in yellow are the overlapping regions in both simulations.

Fig. 4 provides a more comprehensive picture of the fluids' distribution as it demonstrates the spatiotemporal plot of the non-wetting phase saturation at planes perpendicular to the mean direction of the flow S^{yz}_{nw} for (a) $Re_{av} = 1.7 \times 10^{-3}$ and (b) $Re_{av} =$

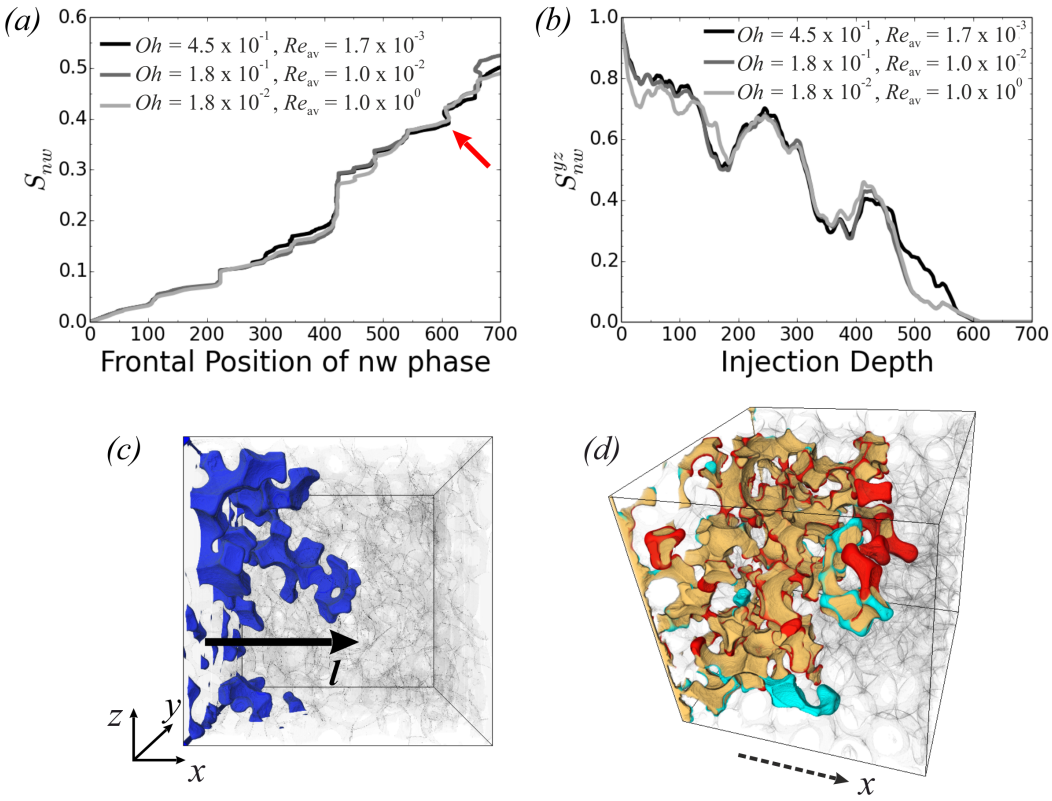

Figure 3. Drainage simulation results at fixed $Ca_{av} = 3.3 \times 10^{-4}$ ($\log M = 0$) and varying Re_{av}, Oh: (a) The non-wetting phase saturation S_{nw} as a function of the frontal position of the non-wetting phase. (b) The non-wetting phase saturation S_{nw}^{yz} at planes perpendicular to the mean direction of the flow for situations with the same total saturation $S_{nw} = 0.3975$ and frontal position $l = 612$ (indicated with the red arrow in (a)). (c) Definition of the frontal position. Non-wetting phase shown in blue, while rock grains and wetting phase are transparent. (d) Comparison of the fluids' configuration for the simulations with $Re_{av} = 1.7 \times 10^{-3}$ and 1.0×10^{-2}. Regions in yellow are occupied by the non-wetting phase in both simulations; regions in light blue are occupied by the non-wetting phase only for the case $Re_{av} = 1.0 \times 10^{-2}$ and regions in red are occupied by the non-wetting phase only for $Re_{av} = 1.7 \times 10^{-3}$.

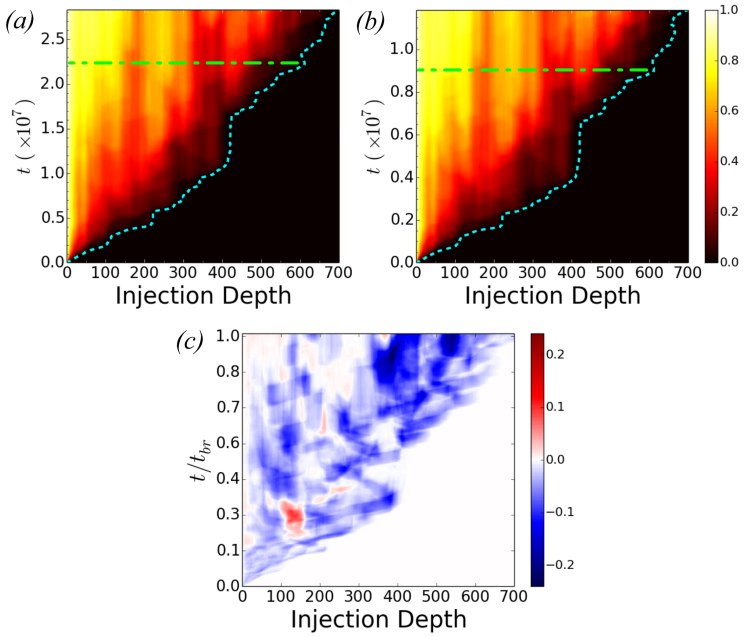

330 **Figure 4.** Spatiotemporal plot of the non-wetting phase saturation S_{nw}^{yz} for drainage sim-
331 ulations at $Ca_{av} \sim 3 \times 10^{-4}$ ($\log M = 0$) and varying Re_{av} and Oh: (a) $Oh = 4.5 \times 10^{-1}$,
332 $Re_{av} = 1.7 \times 10^{-3}$, (b) $Oh = 1.8 \times 10^{-1}$, $Re_{av} = 1.0 \times 10^{-2}$. The injection depth refers to the
333 distance of each yz-plane, at which S_{nw}^{yz} is measured, from the inlet reservoir. The dashed line
334 denotes the frontal position as a function of time, while the dash-dotted line corresponds to the
335 data for S_{nw}^{yz} in Fig. 3(b). (c) The difference between (a) and (b) with red/blue denoting regions
336 with higher S_{nw}^{yz} in (a)/(b). Time is scaled by the time it takes the non-wetting phase to reach
337 the outlet, t_{br}.

1.0×10^{-2}. Although at a first glance these look similar, the differences between the two cases are shown in Fig. 4(c), where red (blue) denotes the regions with higher S_{nw}^{yz} for the case $Re_{av} = 1.7 \times 10^{-3}$(a) ($Re_{av} = 1.0 \times 10^{-2}$(b)). This suggests that the displacement sequence is different. The step-like structure that starts to emerge here for the frontal position (dashed line), as well as in Fig. 3(a) for S_{nw} as a function of time, is a characteristic feature of the capillary fingering regime (Tsuji et al., 2016).

A reasonable question is then "Which one of these simulations is the one that best describes a given drainage situation?". In terms of numerical modeling the question should be rephrased as "What are the relevant dimensionless numbers for the process and the flow regime under investigation?". Matching these dimensionless numbers is essential in capturing the fluid flow behavior. In addressing these questions, it is useful to consider that the ratio of Ca_{av} to Re_{av} is given by the Ohnesorge number, $Oh^2 = Ca_{av}/Re_{av} = \eta_{\mathrm{nw}}^2/(\rho\gamma L_s)$. Oh is a dimensionless number that quantifies the ratio of viscous forces to inertia and interfacial tension. Of particular importance and usefulness in terms of numerical modeling is the fact that the Ohnesorge number is independent of the flow rate (and the externally imposed way to drive the fluid flow). It reflects purely the thermophysical properties of the fluids and the geometry/rock type (McKinley & Renardy, 2011). Therefore, experiments with given fluids and given geometry correspond to constant values of Oh. For example considering the process of geological sequestration of CO_2 (system of CO_2 - brine), Oh varies in the range of $10^{-3} - 10^{-2}$, depending on the choice of the characteristic length-scale L_s of the system. This can be for example the mean radius of the pore throats in a drainage displacement, as the pore throats control the pressure at which pores drain.

Focusing on the case of geological sequestration of CO_2, the important consequence of the above, with regards to numerical modeling, is that inertial effects cannot be neglected for two phase flow at the pore scale as the average Re_{av} is 4 to 6 orders of magnitude higher than the capillary number Ca_{av} ($Oh = sqrt(Ca_{av}/Re_{av}) \sim 10^{-3}$–$10^{-2}$). This is particularly important if we consider flow regimes with Ca_{av} in the range 10^{-7}–10^{-3} and/or flow regimes characterized by sharp interfacial jumps (e.g. Haines jumps), when inertial effects become more profound. Here, for the simulations reported at intermediate $Ca_{av} \sim 3 \times 10^{-4}$, the simulation that would best describe a CO_2 - brine system is the one with $Oh = 1.8 \times 10^{-2}$ ($Re_{av} = 1.0 \times 10^{0}$).

3.1.2 Low Ca_{av} - Haines jumps regime

Extending our investigation to the low Ca_{av} regime, we encounter a transition to a flow regime characterized by Haines jumps. This is evident from the flow field and the inlet-outlet pressure difference, shown in Fig. 5, where we compare simulations at $Oh = 1.8\times10^{-2}$ and varying Ca_{av} (intermediate versus low Ca_{av}). On the left panel we plot the average components of the velocity, while on the right panel the average magnitude of the velocity and the inlet-outlet pressure difference, $\Delta P = P_{inlet} - P_{outlet}$, is shown. A distinct change in both the flow field and the pressure difference is clearly seen: sharp interfacial jumps, indicative of Haines jumps, lead to significant increase of the non-wetting phase velocity and abrupt pressure drops, which coincide with the jumps. The transition to the capillary fingering regime with Haines jumps is also profound by examining the saturation of the injected phase, S_{nw}, as a function of the frontal position, see Fig. 3(a) versus Fig. 6(a). At $Ca_{av} = 3.9 \times 10^{-5}$ the step-like structure of S_{nw} versus frontal position is a consequence of consecutive forward and backward Haines jump events (Tsuji et al., 2016).

For the low Ca_{av} case (fixed average $Ca_{av} = 3.9 \times 10^{-5}$) we examine two situations with $Oh^{(1)} = 1.8 \times 10^{-2}$ ($Re_{av}^{(1)} = 1.6 \times 10^{-1}$) and $Oh^{(2)} = 1.0 \times 10^{-2}$ ($Re_{av}^{(2)} = 3.7\times10^{-1}$) by varying the interfacial tension and the injection flow rate, while the fluids' viscosity remains fixed ($\eta_{\mathrm{nw}} = 6.67\times10^{-3}$). Simulation parameters are as follows: (1) $\gamma^{(1)} = 1.17 \times 10^{-2}$ ($\kappa_\phi = 1 \times 10^{-2}$, $a = -1.54 \times 10^{-2}$), $u_{inj}^{(1)} = 5 \times 10^{-6}$, (2) $\gamma^{(2)} = 3.51 \times 10^{-2}$ ($\kappa_\phi = 3 \times 10^{-2}$, $a = -4.62 \times 10^{-2}$) and $u_{inj}^{(2)} = 1.5 \times 10^{-5}$. Numerically it was not possible to examine situations with a much higher variation in Oh, like the intermediate Ca_{av} case (section 3.1.1) by varying the fluids' viscosity, as this would be computationally very expensive. Given that there is not a significant change in the Ohnesorge number (it could be argued that this corresponds to similar sets of experiments), it would be reasonable to expect that the results reported in Fig. 6 should look similar. The similarity observed in the flow field (Fig. 6(b)) is also an indication that the displacement pathways and the sequence of Haines jumps are the same in both cases. Comparing the fluids' configurations at breakthrough, see Fig. 6(c),(d), reveals that indeed the drainage displacement process is almost similar in both situations, except for mainly a disconnected ganglion (indicated with a red arrow), observed in the case $Oh^{(2)} = 1.0\times 10^{-2}$ ($Re_{av}^{(2)} = 3.7\times10^{-1}$). Interestingly, despite the small difference in Oh, this is the result of distal (non-local) snap-off, that actually persists throughout the simulation time

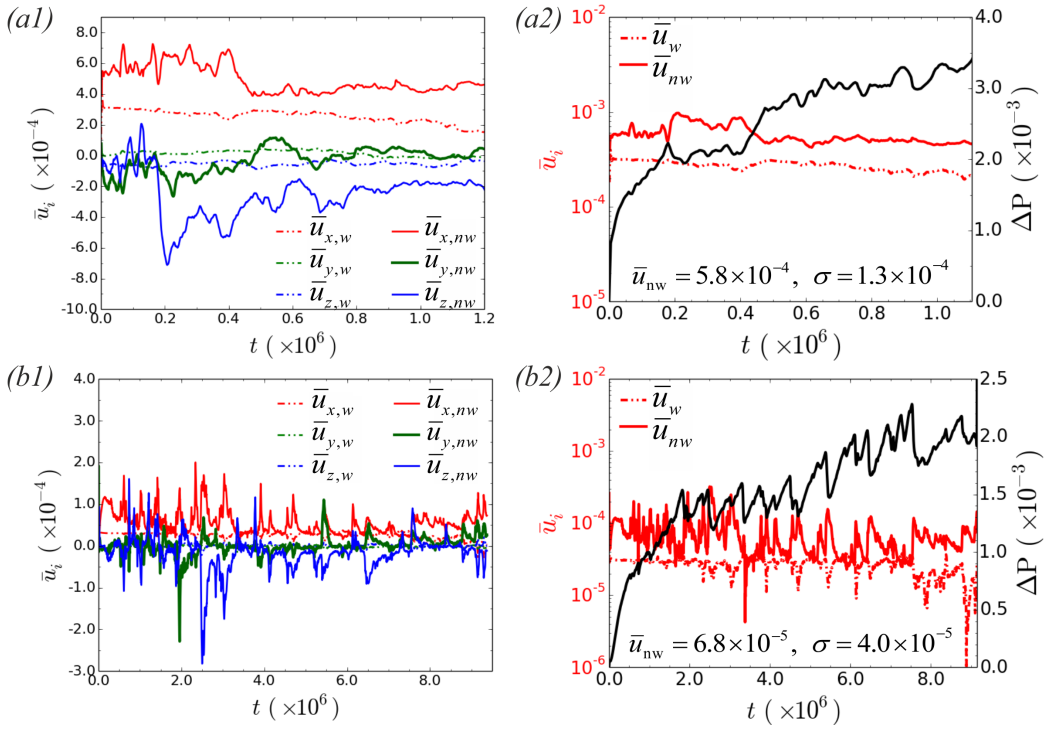

Figure 5. Results from simulations with $Oh = 1.8 \times 10^{-2}$ and: (a) $Ca_{av} = 3.3 \times 10^{-4}$, (b) $Ca_{av} = 3.9 \times 10^{-5}$. Left panel: Average value for the components of the velocity for the wetting/non-wetting phases (dashed/solid lines). Right panel: The corresponding average magnitude of the velocity and inlet-outlet pressure difference. The abrupt pressure drop and the interfacial jumps are indicative of Haines jumps. The occurrence of Haines jumps, as Ca_{av} decreases, is reflected in the distribution of the velocities observed (higher ratio of standard deviation σ to mean velocity $\bar{u}_{\mathrm{nw}}$).

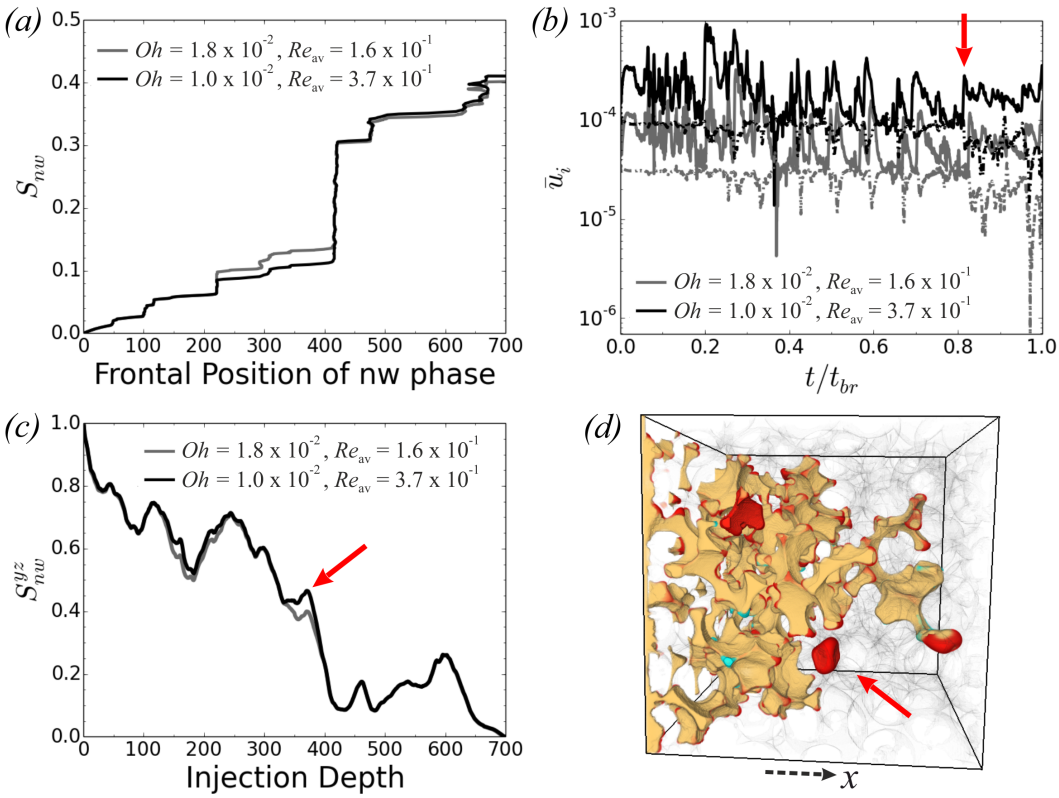

Figure 6. Results from simulations at fixed $Ca_{av} = 3.9 \times 10^{-5}$ and varying Re_{av}, Oh. (a) The non-wetting phase saturation S_{nw} as a function of the frontal position of the non-wetting phase. (b) The average magnitude of the velocity versus time in scaled units $t^* = t/t_{br}$. Solid/dashed lines correspond to the average velocity of the non-wetting/wetting phase. (c) The distribution of the non-wetting phase per injection depth, quantified by S^{yz}_{nw}, at $t = t_{br}$. (d) Visualization of the non-wetting phase configurations at $t = t_{br}$. Regions in yellow are occupied by the non-wetting phase in both simulations; regions in light blue are occupied by the non-wetting phase only for the case $Re_{av} = 1.6 \times 10^{-1}$ ($Oh = 1.8 \times 10^{-2}$) and regions in red are occupied by the non-wetting phase only for $Re_{av} = 3.7 \times 10^{-1}$ ($Oh = 1.0 \times 10^{-2}$). The red arrows indicate the time of distal snap-off (b) and the corresponding disconnected non-wetting phase.

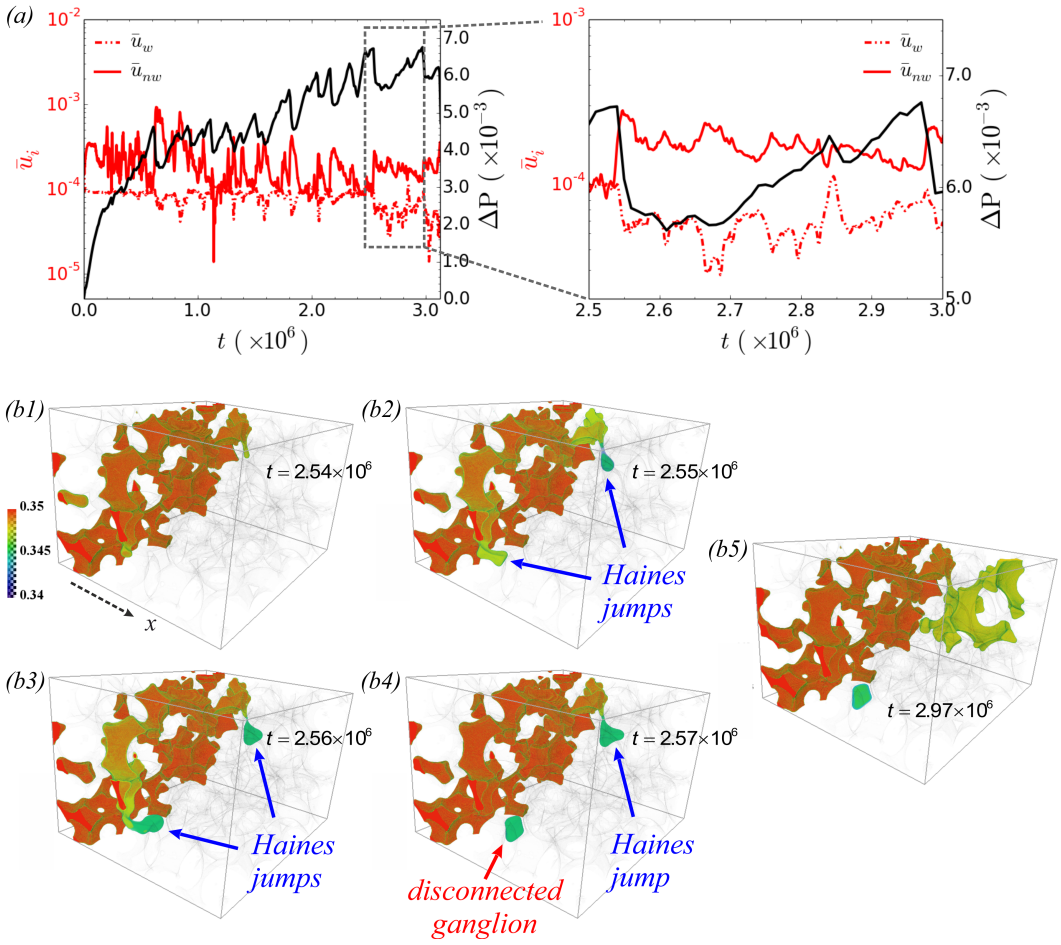

Figure 7. Results from simulations at $Ca_{av} = 3.9 \times 10^{-5}$ and $Oh = 1.0 \times 10^{-2}$. (a) The average magnitude of the velocity versus time and the inlet/outlet pressure difference. Right panel: Zoom in at the times for a jump event that develops distal snap-off. (b) Visualizations of the non-wetting phase displacement that develops distal snap-off event (indicated with the red arrow in (b4)). The non-wetting phase is colored by the bulk pressure to demonstrate the pressure drop during Haines jump events.

and produces a long-lasting fluid configuration (as it remains disconnected) in agreement with the experimental observations of Andrew et al. (2015). Contrarily, local snap-off events generate disconnected fluid configurations that rapidly reconnect with the connected non-wetting phase region (Andrew et al., 2015).

Fig. 7 shows that the distal snap-off event is caused by the transient low dynamic capillary pressure during the abrupt interface movement (high local Re_l), which is then preserved in the capillary pressure of the disconnected ganglion. For the case of $Oh^{(2)} =$

1.0×10^{-2} ($Re_{av}^{(2)} = 3.7 \times 10^{-1}$), the higher interfacial tension affects the dynamics of the Haines jump events, as the higher driving capillary forces result in larger interfacial velocities and pressure drop during the events. Consequently, the bigger reduction in capillary pressure observed, even in throats significantly away from the jump event, can cause the disconnection of the non-wetting phase (distal snap-off). Hence, Ca_{av} and M cannot fully describe a drainage displacement process, even in the low Ca_{av} regime (lower Re_{av}), since the choice of parameters can affect the dynamics of Haines jumps, in which case inertial effects become locally more profound. This results in not capturing the dynamics of Haines jumps and the associated fluids' redistribution (Zacharoudiou et al., 2018). Especially in the case of jumps accompanied with distal snap-off, which can affect the drainage displacement process and the fluids' configuration, since distal snap-off has a persistent impact on the wetting phase flow field and the sequence of subsequent drainage events (Andrew et al., 2015). Moreover, distal snap-off can potentially have a negative impact on the displacement efficiency, which is an extremely significant feature for CO_2 storage and hydrocarbon recovery, as it blocks the access to regions of the pore space that were accessible to the non-wetting phase prior the Haines jump event (Zacharoudiou et al., 2018).

3.2 Local dynamics - Energy conversion during drainage in the low Ca_{av} regime

There is often the argument that two phase flow at the pore scale is at low Reynolds numbers and therefore inertial effects are not important. How small is the average flow Re_{av} has been addressed in the previous section by considering the system's Oh, which links Ca_{av} and Re_{av}. Another question to be addressed is what is the actual local Reynolds number Re_l, especially during jump events and as the average Ca_{av} (Re_{av}) decreases even further, e.g. far away from the injection point. Here we examine the local dynamics and the associated dimensionless numbers (Re_l, Ca_l), during low Ca_{av} flow. To this end we consider simulations with $logM = 0$, $Oh = 1.3 \times 10^{-2}$ and varying Ca_{av}, see Fig. 8. This is achieved by keeping all parameters fixed ($\eta_i = 6.67 \times 10^{-3}$ (i=w, nw), $\gamma = 2.34 \times 10^{-2}$ ($\kappa_\phi = 2 \times 10^{-2}$, $a = -3.08 \times 10^{-2}$), $\theta^{eq} = 40°$) and varying the injection flow rate Q_{inj} ($u_{inj}^{(a)} = 10^{-4}$, $u_{inj}^{(b)} = 10^{-5}$, $u_{inj}^{(c)} = 2 \times 10^{-6}$, $u_{inj}^{(d)} = 2 \times 10^{-7}$). The sharp increase in non-wetting fluid velocity and the decrease in pressure signal observed

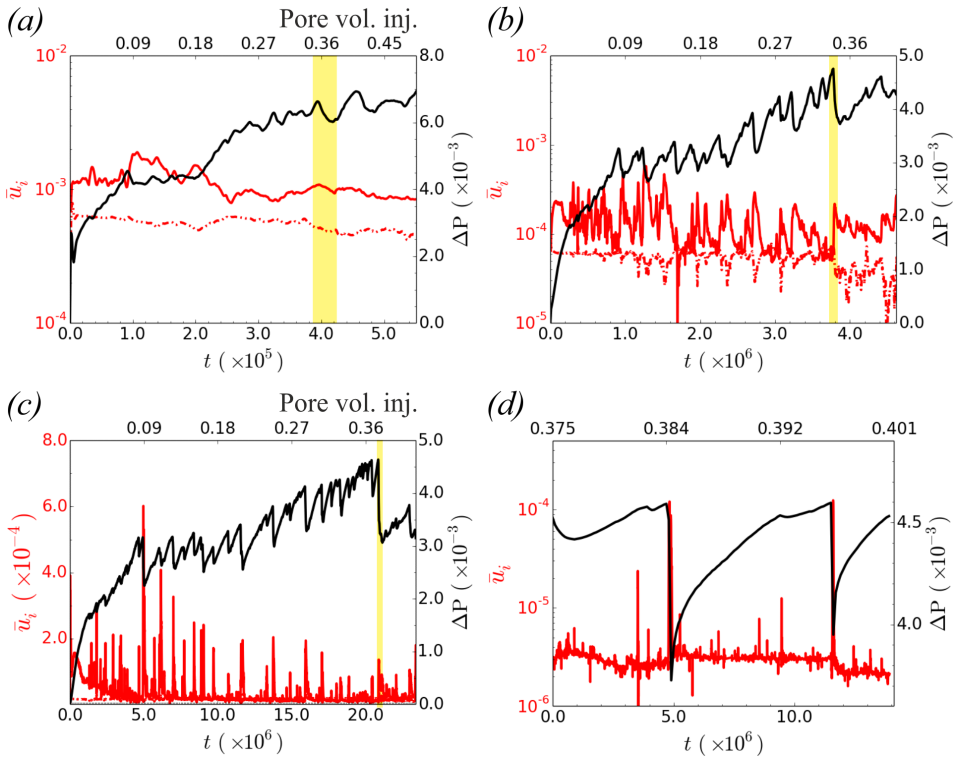

Figure 8. The average magnitude of the velocity for the wetting/non-wetting phase (dashed/solid red lines) and the inlet/outlet pressure difference for simulations with $logM = 0$, $Oh = 1.3 \times 10^{-2}$ and varying Ca_{av}: (a) $Ca_{av} = 3.1 \times 10^{-4}$ ($u_{inj}^{(a)} = 10^{-4}$), (b) $Ca_{av} = 3.8 \times 10^{-5}$ ($u_{inj}^{(b)} = 10^{-5}$), (c) $Ca_{av} = 1.0 \times 10^{-5}$ ($u_{inj}^{(c)} = 2 \times 10^{-6}$) and (d) $Ca_{av} = 1.0 \times 10^{-6}$ ($u_{inj}^{(d)} = 2 \times 10^{-7}$). The yellow shaded regions indicate the time scales of a jump event analysed in Fig.9. Simulation (d) results were obtained from restarting simulation (c) at time $t^{(c)} = 20.08 \times 10^6$ and decreasing the injection flow rate from $u_{inj}^{(c)} = 2 \times 10^{-6}$ to $u_{inj}^{(d)} = 2 \times 10^{-7}$.

for Ca_{av} smaller than $\sim 10^{-5}$, Fig. 8(b)-(d), indicates flow regime with Haines jumps.

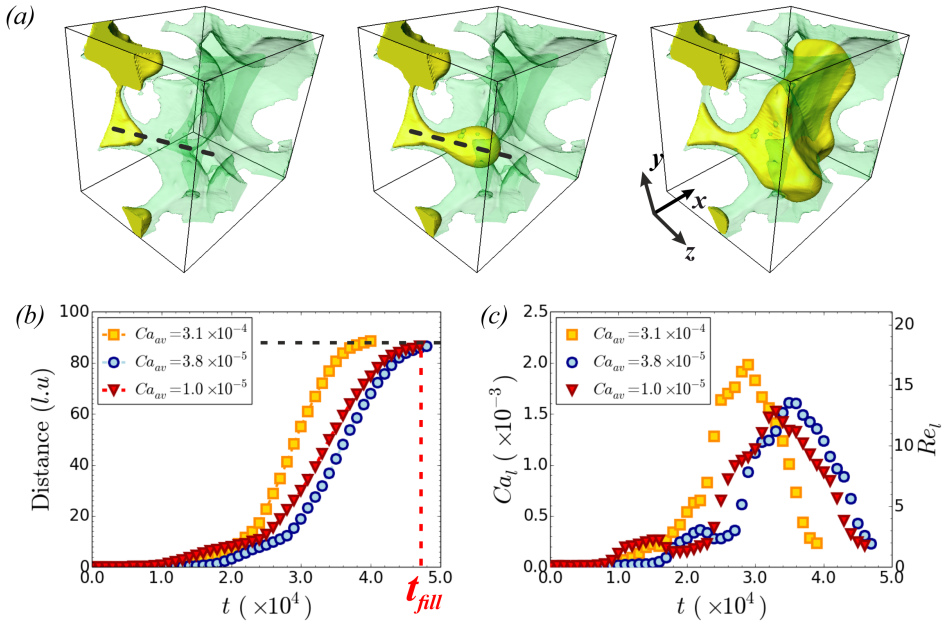

Figure 9. (a) Pore drainage event over multiple geometrically defined pore spaces. The non-wetting invading fluid is shown in yellow. The rock and wetting phase are shown transparent and semi-transparent respectively for effective visualization. (b) The distance traveled by the fluid-fluid interface in the pore space versus time for the simulations reported in Fig. 8(a)-(c). The pore filling time (t_{fill}) can be approximated by the time the interface reached the distance plotted with the horizontal dashed line. (c) The corresponding local dimensionless numbers Ca_l and Re_l using the interfacial velocity obtained from the data in (b). Time $t = 0$ denotes the start of the event.

We focus on a particular drainage event, see Fig. 8(a)-(c) for the time frames considered and Fig. 9 for the draining site. Results presented in Fig. 9(b)-(c) reveal that the jump dynamics (interfacial velocity, pore filling time) in the capillary fingering regime ($Ca_{av} \sim 10^{-5}$) are similar despite a decrease by a factor of 5 in the externally imposed injection flow rate ($u_{inj} = 10^{-5} - Ca_{av} = 3.8 \times 10^{-5}$, $u_{inj} = 2 \times 10^{-6} - Ca_{av} = 1.0 \times 10^{-5}$), in agreement with previous observations (Armstrong & Berg, 2013; Zacharoudiou & Boek, 2016; Li et al., 2019). Moreover, the local maximum $Ca_l \sim 10^{-3}$ and $Re_l \sim 1.5 \times 10^1$ are independent of and orders of magnitude higher than the corresponding average flow values. This holds in general for the jump events (not shown here). Decreas-

ing Ca_{av} to 10^{-6}, see simulation reported in Fig. 8(d), reveals local maximum Reynolds number of the order $Re_l \sim 10^1$. The above indicate that a further decrease in Ca_{av} will not affect the local dynamics (Ca_l, Re_l) significantly, but rather this becomes decoupled from the externally imposed flow rate. More importantly, the local value of Re_l indicates that inertial effects are important and the numerical scheme used should solve the full Navier-Stokes equations, honoring momentum balance, and all relevant forces, i.e., capillary, viscous, and inertial forces acting simultaneously in order to capture the dynamics and the fluid rearrangement during these abrupt events.

The decoupling of local dynamics from the externally imposed flow rate can be understood by considering the energy conversion during drainage. The externally performed work of pressure, $W_p = \int \Delta P Q_{inj} dt$, drives the fluid flow, hence converted to kinetic energy E_k, and stores energy in the system as surface energy F_{surf}. The energy balance states (Ferrari & Lunati, 2014)

$$\frac{dW_p}{dt} - \Phi = \frac{dE_k}{dt} + \frac{dF_{surf}}{dt} \,, \tag{11}$$

where the energy loses are accounted for by the viscous dissipation rate Φ. The change in surface energy is given by $dF_{surf} = \gamma dA_{int} + \gamma_{ws} dA_{ws} + \gamma_{ns} dA_{ns}$, where dA_{int}, dA_{ws} and dA_{ns} are the increments of the areas of the fluid-fluid, solid-wetting fluid and solid - non wetting fluid interfaces respectively and γ, γ_{ws}, γ_{ns} the corresponding surface tensions. Since $dA_{ns} = -dA_{ws}$ and the total solid surface area $A^s_{tot} = A_{ns} + A_{ws}$ is constant, the change in surface energy can be expressed as $dF_{surf} = \gamma(dA_{int} - \cos\theta^{eq} dA_{ws})$. In a drainage situation $dA_{ws} < 0$ and $dA_{int} > 0$; hence, F_{surf} is expected to increase monotonically, except during Haines jumps. In this case, the energetic cost of newly created interfaces ($dA_{int} > 0$) can be balanced due to fluid rearrangement and the released energy due to wetting at the imbibition sites ($dA_{ws} > 0$), leading to a decrease in the overall F_{surf}, see Fig. 10.

Fig. 10 presents results for the time evolution of the interfacial areas and the corresponding change in surface energy for the simulations reported in Fig. 8(a)-(c). The transition to the capillary fingering regime with Haines jumps ($Ca_{av} \sim 10^{-5}$), as the externally imposed flow rate decreases, becomes evident as results demonstrate a higher overlapping degree, but also by examining the monotonicity of the A_{ws} curve in Fig. 10(a). High Ca_{av} flow (smooth flow) leads to a monotonic decrease of A_{ws} (increase of F_{surf}); non-monotonicity emerges with the onset of Haines jumps (burst flow). During the jump

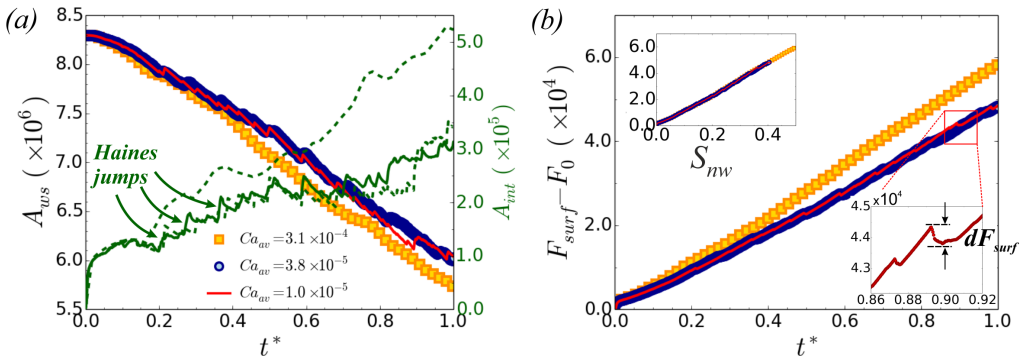

Figure 10. (a) The time evolution of interfacial areas (wetting phase - solid, A_{ws}, fluid-fluid, A_{int}) for simulations with $logM = 0$, $Oh = 1.3 \times 10^{-2}$ and varying Ca_{av}. Time is normalised by the breakthrough time, $t^* = t/t_{br}$. The occurence of Haines jumps is marked with a sharp increase in A_{ws} (imbibition in surrounding pore throats) and A_{int}. Results for A_{int} (green lines): $Ca_{av} = 3.1 \times 10^{-4}$ (dashed line), $Ca_{av} = 3.8 \times 10^{-5}$ (solid line), $Ca_{av} = 1.0 \times 10^{-5}$ (dashed-dotted line). (b) The corresponding surface energy $F_{surf} - F_0$, where $F_0 = \gamma_{ws} A^s_{tot}$ is constant. Inset: (lower right) Surface energy released during Haines jumps; (upper left) surface energy data collapse versus non-wetting phase saturation.

events, the wetting phase-solid interfacial area A_{ws} increases, releasing energy, previously stored in the system, ($dF^{rel}_{surf} = \gamma \cos\theta^{eq} dA_{ws} > 0$) necessary for accelerating the fluids, see sharp peaks in Fig. 8(b)-(c) , and creating new interfaces ($dF^{int}_{surf} = \gamma dA_{int} > 0$). The overlap of the results $F_{surf}(t^*)$ for $Ca_{av} \sim 10^{-5}$ indicates that the distribution of fluids and the displacement sequence is similar despite the decrease in Ca_{av} from 3.8×10^{-5} to 1.0×10^{-5}. The change in injection flow rate affects the rate at which menisci are "charged", but the "discharging" (Haines jumps) is controlled by the amount of energy available (dF^{rel}_{surf}), the viscous dissipation rate, the connectedness of the fluids and the structure of the porous rock. As the externally imposed flow rate decreases, the rate at which energy is provided to the system decreases (dW_p/dt) and, therefore, during the time scales of jump events, the energy balance (eq. 3.1.2) essentially becomes $-\frac{dF_{surf}}{dt} - \Phi = \frac{dE_k}{dt}$. Given that most of the nw phase needed for the draining of the pore body comes from fluid redistribution (Berg et al., 2013; Zacharoudiou et al., 2018), it explains why the local dynamics during jump events, at the same site, becomes decoupled from the externally imposed flow rate, as Ca_{av} decreases beyond a certain limit. See also Fig. 11, where results for the time evolution of the interfacial areas and the sur-

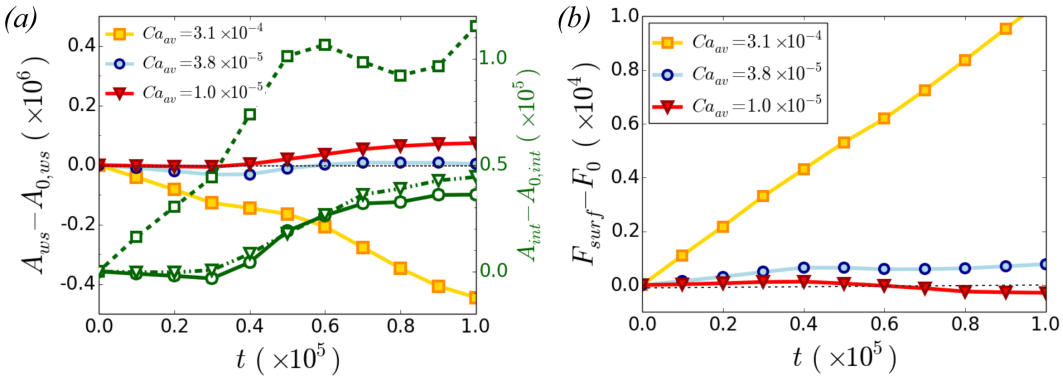

Figure 11. (a) The time evolution of interfacial areas (wetting phase - solid A_{ws}, fluid-fluid A_{int}) during the event shown in Fig. 9(a) and simulations with $logM = 0$, $Oh = 1.3 \times 10^{-2}$ and varying Ca_{av}. $A_{0,ws}$ and $A_{0,int}$ denote the interfacial areas at the start of the event. Results for A_{int} (green lines): $Ca_{av} = 3.1 \times 10^{-4}$ (dashed line), $Ca_{av} = 3.8 \times 10^{-5}$ (solid line), $Ca_{av} = 1.0 \times 10^{-5}$ (dashed-dotted line). (b) The corresponding surface energy $F_{surf} - F_0$, where F_0 is the reference surface energy at the start of the event.

face energy, during the event in Fig. 9(a), start to converge as Ca_{av} decreases from $Ca_{av} = 3.1 \times 10^{-4}$ to 1.0×10^{-5}. Further decrease of the injection flow rate will make the above more profound. Here examining flow regimes with Ca_{av} smaller than 10^{-6} was not possible, as this would have been computationally very costly, given the resources available for this research (8 NVIDIA Tesla P100 GPUs). We must note though, that, to the best of our knowledge, the capillary number flow regimes examined numerically in this manuscript are the lowest reported so far in the literature employing a direct numerical simulation approach.

4 Conclusions

We examine here whether the description of two-phase flow (drainage) in terms of just the capillary number and the viscosity ratio and neglecting inertial effects, based on the pioneering work of Lenormand et al. (1988) and its extension to fully developed drainage by Yortsos et al. (1997), is sufficient to describe the flow at the pore scale correctly. This investigation has obvious implications for large scale numerical modeling of CO_2 geological sequestration and enhanced oil recovery. Especially, considering the fact that the acceleration of numerical algorithms using GPGPUs can enable the study of two phase flow at the pore-scale at smaller capillary numbers Ca_{av} than what was possible

so far. We essentially examine whether direct numerical simulation approaches need to solve the full Navier Stokes equations and consider all relevant forces, i.e. capillary, viscous and inertial forces, acting simultaneously, in order to capture the physics of fluid-fluid displacement and interfacial phenomena at the pore scale.

Given the range of the relevant dimensionless numbers in porous media flows, and especially the ratio of viscous to capillary forces, $10^{-10} < Ca_{av} < 10^{-3}$, depending on the distance from the injection point in the well bore (Blunt & Scher, 1995), we examined two test cases at intermediate ($Ca_{av} \sim 10^{-4}$) and low capillary numbers ($Ca_{av} \sim 10^{-5}$). A distinct change in the flow regime is observed between the above two situations, as the later is characterised by abrupt jumps in the location of the fluid-fluid interface (Haines jumps), expected for low Ca_{av} flow. Our investigation clearly shows that inertial effects cannot be neglected in neither of the two flow regimes, i.e. we cannot examine the fluid flow as being in the limit of zero Reynolds number. Generally two-phase flow at the pore scale is assumed to be at low Re_{av}. How small, though, is Re_{av}, can be answered by examining the Ohnesorge number ($Oh^2 = Ca_{av}/Re_{av}$). This dimensionless number is fixed for a given system and reflects the thermophysical properties of the specific system under investigation, i.e. the fluids' properties and the length scale dependencies originating from the porous medium geometry. Considering that Oh is typically in the range of 10^{-3}-10^{-2} for a system of brine-CO_2 at the pore scale, i.e. Re_{av} is 4 to 6 orders of magnitude higher than Ca_{av}, it becomes clear that the usual approach in numerical simulations of keeping both Ca_{av} and Re_{av} low, without respecting the ratio of the two, is fundamentally wrong, especially for the intermediate Ca_{av} flow regime.

As Ca_{av} and Re_{av} decrease further, inertial effects are still important over a transient amount of time during abrupt jump events (Haines jumps), when the non-wetting phase passes from a narrow restriction to a wider pore body. Our results demonstrate that local jump dynamics become decoupled from the externally imposed flow rate, and locally Ca_l and Re_l are orders of magnitude higher than the average corresponding values. Moreover, the displacement sequence as well as the fluids' distribution in the porous rock can be affected significantly by the choice of the simulation parameters. Therefore, matching the system's Oh, as well as using a Navier-Stokes solver are essential in resolving the fluid dynamics during these abrupt events and capturing the fluids' spatial distribution/connectedness, given that significant fluid rearrangement takes place. Otherwise the predicting capabilities of the numerical scheme should be questioned. In terms

of numerical modeling, fixing Oh based on fluid properties and characteristic length scales, provides a convenient way of restricting the parameter selection process.

Finally, it would be interesting to examine how the consideration of: (a) Haines jumps and inertial effects occurring on a single and/or multiple pore levels and (b) snap-off events, both distally and locally, alter in a macroscopic sense the invasion percolation aspects of a drainage process, e.g. sign and gradient of percolation probability, or the transition between the macrosscopically observed flow regimes, as captured by the Lenormand phase diagram (Lenormand et al., 1988) and in its extension to fully-developed drainage by Yortsos et al. (1997). This remains a challenge left for future studies.

Appendix A Lattice Boltzmann Method

Here we provide details on the implementation of the free energy lattice Boltzmann (Swift et al., 1995, 1996; Briant & Yeomans, 2004; Krüger et al., 2017) algorithm we use to solve the hydrodynamic equations of motion, the continuity and Navier Stokes equations coupled to an advection diffusion equation for the order parameter (composition). The dynamics are introduced by discretised Boltzmann equations for two sets of distribution functions, $f_i(\mathbf{r},t)$, $g_i(\mathbf{r},t)$, which are related to the local fluid density $\sum_i f_i(\mathbf{r},t) = \rho$ and order parameter $\sum_i g_i(\mathbf{r},t) = \phi$ Collision step: $\mathrm{f}_i'(\mathbf{r},t) = f_i(\mathbf{r},t)+\Omega_{f,i}(\mathbf{r},t)$,

$\mathrm{g}_i'(\mathbf{r},t) = g_i(\mathbf{r},t) + \Omega_{g,i}(\mathbf{r},t)$,

Propagation step: $\mathrm{f}_i(\mathbf{r}+\mathbf{e_i}\Delta t, t+\Delta t) = f_i'(\mathbf{r},t)$,

$\mathrm{g}_i(\mathbf{r}+\mathbf{e_i}\Delta t, t+\Delta t) = g_i'(\mathbf{r},t)$, The distribution functions are discrete in time and space, with the time step Δt and lattice spacing Δx being set to unity. The subscript i refers to the discrete set of velocity directions $\{\mathbf{e_i}\}$. Here we use a three dimensional model with 19 discrete velocity vectors (D3Q19). Eq. Appendix A states that the time evolution of the distribution functions proceeds as follows: a) a collision step described by the collision operator $\Omega_{f/g,i}$ and b) a propagation step with velocity $\mathbf{e_i}$ to the neighbouring lattice point $\mathbf{r}+\mathbf{e_i}\Delta t$ at the next time step $t+\Delta t$. In a concise form, the lattice Boltzmann equation, for f_i for example, becomes $f_i(\mathbf{r}+\mathbf{e_i}\Delta t, t+\Delta t) = f_i(\mathbf{r},t)+\Omega_{f,i}(\mathbf{r},t)$.

The collision operators $\Omega_{f,i} = -M^{-1}SM[f_i(\mathbf{r},t) - f_i^{eq}(\mathbf{r},t)]$,

$\Omega_{g,i} = -\frac{\Delta t}{\tau_g}[g_i(\mathbf{r},t) - g_i^{eq}(\mathbf{r},t)]$, relax the distribution functions to their equilibrium values (f_i^{eq}, g_i^{eq}) with relaxation time scales $\tau_{f,j}$ ($j = w, nw$) and τ_g. These re-

laxation times are related to the transport coefficients, dynamic viscosity η_j $(j = w, nw)$ and mobility M_ϕ in the hydrodynamic equations via $\eta_j = \rho c^2 \Delta t\big(\tau_{f,j} - 1/2\big)/3$,

$\mathrm{M}_\phi = \Delta t\, \Gamma\big(\tau_g - 1/2\big)$, where $c = \Delta x/\Delta t$ and Γ is a tunable parameter in the equilibrium distribution functions g_i^{eq}, see eq. A4. By expanding the chemical potential μ in powers of $\phi - \phi_{eq}$, for small deviations from equilibrium,

$$\mu = (a + 3b\phi_{eq}^2)(\phi - \phi_{eq}) + O((\phi - \phi_{eq})^2) \,, \tag{A1}$$

the diffusive term $M_\phi \nabla^2 \mu$ in the convection-diffusion eq. 9 can be written as $D\nabla^2\phi$ with $D = M_\phi(a + 3b\phi_{eq}^2)$ the diffusion coefficient. We note here that it is also possible to define the mobility coefficient M_ϕ to be a function of the order parameter ϕ in such a way that is restricting diffusion to the vicinity of fluid-fluid interfaces (F. O. Alpak et al., 2019).

In order to improve accuracy and stability, we adopt a Multiple Relaxation Time (MRT) (D'Humières et al., 2002) approach for the evolution of the distribution functions $f_i's$, associated with the fluid density ρ, meaning that different relaxation rates are adopted for different linear combinations of the distribution functions (moments of $f_i's$). The matrix M performs a transformation, so that collisions are performed in moment space. First the $f_i's$ are mapped to moment space, then the moments are relaxed towards equilibrium, and finally the relaxed moments are mapped back to population space. The information for the relaxation rates, $\omega = 1/\tau$, for the different linear combinations of the distribution functions (moments of $f_i's$) is contained in the relaxation matrix S. Following (C. Pooley et al., 2009), the relaxation times responsible for generating the viscous terms in the Navier-Stokes equation are set to τ_f, those related to conserved quantities to infinity and all the others, which correspond to non-hydrodynamic modes, to unity. On the other hand, a single relaxation time approximation is sufficient for the $g_i's$, given that the mobility coefficient M_ϕ in Eq. eq:advection$_d$$if fusion_e$$qcanbetunedbytheindependentparameter\Gamma$ through eq. eq:Mobility. This allows us to fix the relaxation time $\tau_g = 1$. As shown by C. Pooley et al. (2009), this approach suppresses spurious currents at the contact line, while improving significantly the numerical stability of the algorithm as well (Lallemand & Luo, 2000). Throughout this work we choose a relative small value for $\Gamma = 1.0$ and refer the reader to the work by Ledesma-Aguilar et al. (2007) on how this (Γ and consequently the diffusion coefficient D) affects the contact line motion. Given the low Ca_{av} flow examined in this work, any wetting films adhered to the side walls are very small in size (less than 1% of the channel width) (Ledesma-Aguilar et al., 2007). Hence, in-

vaded pore spaces are fully occupied by the injected non-wetting phase and the value for Γ is not affecting the results.

The moments of the distribution functions are related to the physical quantities, mass density ρ, momentum density $\rho\mathbf{u}$ and composition

$$\sum_{i=0}^{18} f_i = \rho, \qquad \sum_{i=0}^{18} f_i e_{i\alpha} = \rho u_\alpha \ , \qquad \sum_{i=0}^{18} g_i = \phi \ . \tag{A2}$$

The equilibrium distributions functions are defined as a power series in the velocity (C. M. Pooley & Furtado, 2008)

$$f_i^{eq} = w_i c^2 \left(p_b - \kappa_\phi \nabla^2 \phi + e_{i\alpha} \rho u_\alpha + 32 c^2 \left[e_{i\alpha} e_{i\beta} - c^2 3 \delta_{\alpha\beta} \right] \rho u_\alpha u_\beta \right)$$
$$+ \kappa_\phi c^2 \left(w_i^{xx} \partial_x \phi \partial_x \phi + w_i^{yy} \partial_y \phi \partial_y \phi + w_i^{zz} \partial_z \phi \partial_z \phi \right.$$
$$\left. + w_i^{xy} \partial_x \phi \partial_y \phi + w_i^{xz} \partial_x \phi \partial_z \phi + w_i^{yz} \partial_y \phi \partial_z \phi \right) \ , \tag{A3}$$

$$g_i^{eq} = w_i c^2 \left(\Gamma \mu + e_{i\alpha} \phi u_\alpha + 32 c^2 \left[e_{i\alpha} e_{i\beta} - c^2 3 \delta_{\alpha\beta} \right] \phi u_\alpha u_\beta \right), \tag{A4}$$

with the coefficients (C. M. Pooley & Furtado, 2008) $\mathrm{w}_{1-6} = 16,\ w_{7-18} = 112,$

$\mathrm{w}_{1,2}^{xx} = w_{3,4}^{yy} = w_{5,6}^{zz} = 512,$

$\mathrm{w}_{3-6}^{xx} = w_{1,2,5,6}^{yy} = w_{1-4}^{zz} = -13,$

$\mathrm{w}_{7-10}^{xx} = w_{15-18}^{xx} = w_{7-14}^{yy} = w_{11-18}^{zz} = -124,$

$\mathrm{w}_{11-14}^{xx} = w_{15-18}^{yy} = w_{7-10}^{zz} = 112,$

$\mathrm{w}_{1-6}^{xy} = w_{1-6}^{yz} = w_{1-6}^{xz} = 0,$

$\mathrm{w}_{7,10}^{xy} = w_{11,14}^{yz} = w_{15,18}^{xz} = 14,$

$\mathrm{w}_{8,9}^{xy} = w_{12,13}^{yz} = w_{16,17}^{xz} = -14,$

$\mathrm{w}_{11-18}^{xy} = w_{7-10}^{yz} = w_{15-18}^{yz} = w_{7-14}^{xz} = 0.$ The values for $i = 0$ are chosen to conserve the local mass and composition $\mathrm{f}_0^{eq} = \rho - \sum_{i \neq 0} f_i$,

$\mathrm{g}_0^{eq} = \phi - \sum_{i \neq 0} g_i$, The above choice for the coefficients in eqs. eq:f$_e quil_d istr -$ $eq : def_e q_d istr_g isnotunique; itwasshownthoughtoreducetheunphysicalcurrents, calledspuriousvelocities, thatappearc$ and the Laplacian ($\nabla^2 \phi$) that appear in the equilibrium distribution functions and the chemical potential, using stencils (discrete operators).

The hydrodynamic equations of motion, continuity eq:continuity, Navier-Stokes eq:Navier-Stokes and convection diffusion equation eq:advection$_d if fusion_e q, canbeobtainedbyperformingaChapman-$

$Enskogexpansion(Luo,2000)onthediscretisedBoltzmannequations(eq.\ eq:evolution_distr_funct),whilethefollowingr$

$$\rho\ , \qquad \sum_{i=0}^{18} f_i^{eq} e_{i\alpha} = \rho u_\alpha, \qquad \sum_{i=0}^{18} f_i^{eq} e_{i\alpha} e_{i\beta} = P_{\alpha\beta} + \rho u_\alpha u_\beta\ ,$$

$$\sum_{i=0}^{18} f_i^{eq} e_{i\alpha} e_{i\beta} e_{i\gamma} = \frac{\rho c^2}{3}\Big(u_\alpha \delta_{\beta\gamma} + u_\beta \delta_{\alpha\gamma} + u_\gamma \delta_{\alpha\beta}\Big)\ ,$$

$$\sum_{i=0}^{18} g_i^{eq} = \phi, \qquad \sum_{i=0}^{18} g_i^{eq} e_{i\alpha} = \phi u_\alpha, \qquad \sum_{i=0}^{18} g_i^{eq} e_{i\alpha} e_{i\beta} = \Gamma\mu\delta_{\alpha\beta} + \phi u_\alpha u_\beta\ .$$

Finally we would like to point out that the free energy lattice Boltzmann method is capable of handling high viscosity ratios up to 10^3. For validation of the numerical method we refer the reader to the work reported in (Zacharoudiou & Boek, 2016; Zacharoudiou et al., 2017; F. O. Alpak et al., 2019). This covers the dynamics of capillary filling, demonstrating that the method can capture the correct dynamics of imbibition in the limits of short and long time scales (different regimes for the imbibition length Vs time), as well as for varying viscosity ratio (we considered viscosity ratios $M = \eta_{\rm nw}/\eta_{\rm w}$ in the range $10^{-3} \leq M \leq 1$) (Zacharoudiou & Boek, 2016). The scaling of the dynamic contact angle with the interface velocity (capillary number) was found to be in excellent agreement with Cox theoretical prediction (Cox, 1986) for both 2D simulations (Zacharoudiou & Boek, 2016) and 3D channels with a rectangular cross-section (Zacharoudiou et al., 2017). The method was also shown to correctly predict fluid connectivity in imbibition in Gildehauser sandstone and simulate relative permeability data in close agreement with results from Darcy-scale core flooding experiments (F. Alpak et al., 2018). Further validation of the method investigating snap-off in constricted capillary tubes, Haines jumps and capillary desaturation on real-rock systems is reported in (F. O. Alpak et al., 2019).

A1 Boundary Conditions

In the lattice Boltzmann method we encounter three types of boundary conditions: a) the no-slip boundary condition on the velocity field b) the wetting boundary condition, eq. 5, on the composition and c) the boundary conditions at the inlet-outlet of the simulation domain that is related to how the fluid flow is driven.

The no-slip boundary condition, referring to the condition at solid boundaries where the fluid has zero velocity relative to the boundary, is implemented using the midlink

bounce-back method proposed by Ladd and Verberg (2001). Incoming populations are reflected back towards the lattice nodes they came from, resulting in recovering the wall location (zero velocity) half-way between the fluid and solid node.

Regarding the implementation of the wetting boundary condition, eq. eq:wet$_b$*cdefinesthevalueofthenormalderi* at the substrate in equilibrium. Using this condition and the values for the composition ϕ at the fluid nodes neighbouring the boundary we assign the appropriate values for ϕ at the solid boundary nodes following Niu et al. (2007). The main advantage of this method is that the terms $\partial_\alpha \phi$ and $\nabla^2 \phi$, needed for the evaluation of f_i^{eq} and g_i^{eq} in eqs. eq:f$_e$*quil$_d$istr, eq* : *def$_e$q$_d$istr$_g$, canbeca*

Finally, we choose to drive the fluid flow by applying a constant injection flow rate, i.e. applying velocity boundary conditions at the inlet/outlet of the simulation domain. In particular we adopt the approach proposed by Hecht and Harting (2010) to two-phase flow to estimate the missing populations (f_i, g_i) at the inlet/outlet domain boundaries. The above choice of driving the fluid flow enables the study of the low Ca_{av} flow regime characterised by Haines jumps, which wouldn't be possible in an alternative scenario of using a body force (pressure gradient) to drive the fluid flow (Zacharoudiou et al., 2018).

Acknowledgments

The data reported in the manuscript had been deposited in the UK Carbon Capture and Storage Research Centre (UKCCSRC) Data and Information Archive (DOI: 10.5285/500298bb-baf4-45b9-8a81-e3e0f93891e6). This work was conducted as part of the Qatar Carbonates and Carbon Storage Research Centre (QCCSRC), jointly funded by Qatar Petroleum, Shell and the Qatar Science and Technology Park.

References

Alpak, F., Berg, S., & Zacharoudiou, I. (2018). Prediction of fluid topology and relative permeability in imbibition in sandstone rock by direct numerical simulation. *Advances in Water Resources*, *122*, 49 - 59. doi: https://doi.org/10.1016/j.advwatres.2018.09.001

Alpak, F. O., Zacharoudiou, I., Berg, S., Dietderich, J., & Saxena, N. (2019). Direct simulation of pore-scale two-phase visco-capillary flow on large digital rock images using a phase-field lattice Boltzmann method on general-purpose graphics

processing units. *Computational Geosciences*. doi: 10.1007/s10596-019-9818-0

Anderson, D. M., McFadden, G. B., & Wheeler, A. A. (1998). Diffuse-interface methods in fluid mechanics. *Annual Review of Fluid Mechanics*, *30*(1), 139-165. doi: 10.1146/annurev.fluid.30.1.139

Andrew, M., Bijeljic, B., & Blunt, M. (2014). Pore-scale contact angle measurements at reservoir conditions using X-ray microtomography. *Advances in Water Resources*, *68*, 24 - 31. doi: http://doi.org/10.1016/j.advwatres.2014.02.014

Andrew, M., Menke, H., Blunt, M., & Bijeljic, B. (2015). The Imaging of Dynamic Multiphase Fluid Flow Using Synchrotron-Based X-ray Microtomography at Reservoir Conditions. *Transport in Porous Media*, *110*(1), 1–24. doi: 10.1007/s11242-015-0553-2

Armstrong, R. T., & Berg, S. (2013). Interfacial velocities and capillary pressure gradients during Haines jumps. *Physical Review E*, *88*(4), 043010. doi: 10.1103/PhysRevE.88.043010

Armstrong, R. T., Evseev, N., Koroteev, D., & Berg, S. (2015). Modeling the velocity field during Haines jumps in porous media. *Advances in Water Resources*, *77*(0), 57 - 68. doi: 10.1016/j.advwatres.2015.01.008

Benzi, R., Succi, S., & Vergassola, M. (1992). The lattice Boltzmann equation: theory and applications. *Physics Reports*, *222*(3), 145–197. doi: 10.1016/0370-1573(92)90090-M

Berg, S., Ott, H., Klapp, S. A., Schwing, A., Neiteler, R., Brussee, N., ... Stampanoni, M. (2013). Real-time 3D imaging of Haines jumps in porous media flow. *Proceedings of the National Academy of Sciences*, *110*(10), 3755-3759. doi: 10.1073/pnas.1221373110

Blunt, M. J., & Scher, H. (1995). Pore-level modeling of wetting. *Physical Review E*, *52*(6), 6387. doi: 10.1103/PhysRevE.52.6387

Briant, A. J., Wagner, A. J., & Yeomans, J. M. (2004). Lattice Boltzmann simulations of contact line motion. I. Liquid-gas systems. *Phys. Rev. E*, *69*(3), 031602. doi: 10.1103/PhysRevE.69.031602

Briant, A. J., & Yeomans, J. M. (2004). Lattice Boltzmann simulations of contact line motion. II. Binary fluids. *Phys. Rev. E*, *69*(3), 031603. doi: 10.1103/PhysRevE.69.031603

Cahn, J. (1977). Critical-Point Wetting. *J. Chem. Phys.*, *66*, 3367. doi: 10.1063/1

.434402

Chen, S., Wang, Z., Shan, X., & Doolen, G. D. (1992). Lattice Boltzmann computational fluid dynamics in three dimensions. *Journal of Statistical Physics*, *68*(3-4), 379–400. doi: 10.1007/BF01341754

Chen, Y., Li, Y., Valocchi, A. J., & Christensen, K. T. (2018). Lattice Boltzmann simulations of liquid CO_2 displacing water in a 2D heterogeneous micromodel at reservoir pressure conditions. *Journal of Contaminant Hydrology*, *212*, 14 - 27. doi: 10.1016/j.jconhyd.2017.09.005

Cox, R. G. (1986). The dynamics of the spreading of liquids on a solid surface. Part 1. Viscous flow. *Journal of Fluid Mechanics*, *168*, 169–194. doi: 10.1017/S0022112086000332

de Gennes, P. G. (1985, Jul). Wetting: statics and dynamics. *Rev. Mod. Phys.*, *57*(3), 827–863. doi: 10.1103/RevModPhys.57.827

D'Humières, D., Ginzburg, I., Krafczyk, M., Lallemand, P., & Luo, L.-S. (2002). Multiple-relaxation-time lattice Boltzmann models in three dimensions. *Royal Society of London Philosophical Transactions Series A*, *360*, 437. doi: 10.1098/rsta.2001.0955

Dong, H., & Blunt, M. (2009, Sep). Pore-network extraction from micro-computerized-tomography images. *Phys. Rev. E*, *80*, 036307. doi: 10.1103/PhysRevE.80.036307

Doolen, G. (1990). *Lattice gas methods for partial differential equations: a volume of lattice gas reprints and articles, including selected papers from the Workshop on Large Nonlinear Systems, held August, 1987 in Los Alamos, New Mexico* (Vol. 4). Addison-Wesley Longman.

Ferrari, A., & Lunati, I. (2014). Inertial effects during irreversible meniscus reconfiguration in angular pores. *Advances in Water Resources*, *74*, 1 - 13. doi: 10.1016/j.advwatres.2014.07.009

Hecht, M., & Harting, J. (2010). Implementation of on-site velocity boundary conditions for D3Q19 lattice Boltzmann simulations. *Journal of Statistical Mechanics: Theory and Experiment*, *2010*(01), P01018. doi: 10.1088/1742-5468/2010/01/P01018

Jacqmin, D. (2000). Contact-line dynamics of a diffuse fluid interface. *Journal of Fluid Mechanics*, *402*, 57-88. doi: 10.1017/S0022112099006874

Kazemifar, F., Blois, G., Kyritsis, D. C., & Christensen, K. T. (2016). Quantifying the flow dynamics of supercritical CO_2-water displacement in a 2D porous micromodel using fluorescent microscopy and microscopic PIV. *Advances in Water Resources*, *95*, 352 - 368. (Pore scale modeling and experiments) doi: 10.1016/j.advwatres.2015.05.011

Kendon, V., Cates, M., Pagonabarraga, I., Desplat, J.-C., & Bladon, P. (2001, 8). Inertial effects in three-dimensional spinodal decomposition of a symmetric binary fluid mixture: a lattice Boltzmann study. *Journal of Fluid Mechanics*, *440*, 147–203. doi: 10.1017/S0022112001004682

Krüger, T., Kusumaatmaja, H., Kuzmin, A., Shardt, O., Silva, G., & Viggen, E. M. (2017). The lattice Boltzmann method. *Springer International Publishing*, *10*, 978–3. doi: 10.1007/978-3-319-44649-3

Ladd, A. J. C., & Verberg, R. (2001). Lattice-Boltzmann Simulations of Particle-Fluid Suspensions. *J. Stat. Phys.*, *104*, 1191. doi: 10.1023/A:1010414013942

Lallemand, P., & Luo, L.-S. (2000). Theory of the lattice Boltzmann method: Dispersion, dissipation, isotropy, Galilean invariance, and stability. *Physical Review E*, *61*, 6546–6562. doi: 10.1103/PhysRevE.61.6546

Ledesma-Aguilar, R., Hernández-Machado, A., & Pagonabarraga, I. (2007). Three-dimensional aspects of fluid flows in channels. I. Meniscus and thin film regimes. *Physics of Fluids*, *19*(10), 102112. doi: 10.1063/1.2801511

Lenormand, R., Touboul, E., & Zarcone, C. (1988). Numerical models and experiments on immiscible displacements in porous media. *Journal of Fluid Mechanics*, *189*, 165-187. doi: 10.1017/S0022112088000953

Li, Y., Blois, G., Kazemifar, F., & Christensen, K. T. (2019). High-Speed Quantification of Pore-Scale Multiphase Flow of Water and Supercritical CO2 in 2-D Heterogeneous Porous Micromodels: Flow Regimes and Interface Dynamics. *Water Resources Research*, *55*(5), 3758-3779. doi: 10.1029/2018WR024635

Li, Y., Kazemifar, F., Blois, G., & Christensen, K. T. (2017). Micro-PIV measurements of multiphase flow of water and liquid CO_2 in 2-D heterogeneous porous micromodels. *Water Resources Research*, *53*(7), 6178-6196. doi: 10.1002/2017WR020850

Luo, L.-S. (2000). Theory of the lattice Boltzmann method: Lattice Boltzmann models for nonideal gases. *Phys. Rev. E*, *62*, 4982–4996. doi:

10.1103/PhysRevE.62.4982

McKinley, G., & Renardy, M. (2011). Wolfgang von Ohnesorge. *Physics of Fluids*, *23*(12), 127101. doi: 10.1063/1.3663616

Moebius, F., & Or, D. (2012). Interfacial jumps and pressure bursts during fluid displacement in interacting irregular capillaries. *Journal of Colloid and Interface Science*, *377*(1), 406 - 415. doi: 10.1016/j.jcis.2012.03.070

Moebius, F., & Or, D. (2014). Inertial forces affect fluid front displacement dynamics in a pore-throat network model. *Phys. Rev. E*, *90*, 023019. doi: 10.1103/PhysRevE.90.023019

Niu, X.-D., Munekata, T., Hyodo, S.-A., & Suga, K. (2007). An investigation of water-gas transport processes in the gas-diffusion-layer of a PEM fuel cell by a multiphase multiple-relaxation-time lattice Boltzmann model. *Journal of Power Sources*, *172*(2), 542 - 552. doi: 10.1016/j.jpowsour.2007.05.081

Pierre, & Seppecher. (1996). Moving contact lines in the Cahn-Hilliard theory. *International Journal of Engineering Science*, *34*(9), 977 - 992. doi: 10.1016/0020-7225(95)00141-7

Pooley, C., Kusumaatmaja, H., & Yeomans, J. (2009). Modelling capillary filling dynamics using lattice Boltzmann simulations. *The European Physical Journal-Special Topics*, *171*(1), 63–71. doi: 10.1140/epjst/e2009-01012-0

Pooley, C. M., & Furtado, K. (2008, Apr). Eliminating spurious velocities in the free-energy lattice Boltzmann method. *Phys. Rev. E*, *77*, 046702. doi: 10.1103/PhysRevE.77.046702

Rabbani, H. S., Joekar-Niasar, V., Pak, T., & Shokri, N. (2017). New insights on the complex dynamics of two-phase flow in porous media under intermediate-wet conditions. *Scientific reports*, *7*(1), 4584. doi: 10.1038/s41598-017-04545-4

Raeini, A., Blunt, M., & Bijeljic, B. (2014). Direct simulations of two-phase flow on micro-CT images of porous media and upscaling of pore-scale forces. *Advances in Water Resources*, *74*, 116 - 126. doi: 10.1016/j.advwatres.2014.08.012

Shah, S., Crawshaw, J., Gray, F., Yang, J., & Boek, E. (2017). Convex hull approach for determining rock representative elementary volume for multiple petrophysical parameters using pore-scale imaging and Lattice-Boltzmann modelling. *Advances in Water Resources*, *104*(Supplement C), 65 - 75. doi: 10.1016/j.advwatres.2017.03.008

Shah, S., Gray, F., Crawshaw, J., & Boek, E. (2016). Micro-computed tomography pore-scale study of flow in porous media: Effect of voxel resolution. *Advances in Water Resources*, *95*(Supplement C), 276 - 287. doi: 10.1016/j.advwatres.2015.07.012

Singh, K., Scholl, H., Brinkmann, M., Di Michiel, M., Scheel, M., Herminghaus, S., & Seemann, R. (2017). The role of local instabilities in fluid invasion into permeable media. *Scientific reports*, *7*(1), 444. doi: https://doi.org/10.1038/s41598-017-00191-y

Succi, S. (2001). *The Lattice-Boltzmann Equation*. Oxford university press, Oxford.

Swift, M. R., Orlandini, E., Osborn, W. R., & Yeomans, J. M. (1996, Nov). Lattice Boltzmann simulations of liquid-gas and binary fluid systems. *Phys. Rev. E*, *54*(5), 5041–5052. doi: 10.1103/PhysRevE.54.5041

Swift, M. R., Osborn, W. R., & Yeomans, J. M. (1995, Jul). Lattice Boltzmann simulation of nonideal fluids. *Phys. Rev. Lett.*, *75*(5), 830–833. doi: 10.1103/PhysRevLett.75.830

Tsuji, T., Jiang, F., & Christensen, K. (2016). Characterization of immiscible fluid displacement processes with various capillary numbers and viscosity ratios in 3D natural sandstone. *Advances in Water Resources*, *95*, 3 - 15. doi: http://doi.org/10.1016/j.advwatres.2016.03.005

Yamabe, H., Tsuji, T., Liang, Y., & Matsuoka, T. (2015). Lattice Boltzmann Simulations of Supercritical CO_2 - Water Drainage Displacement in Porous Media: CO_2 Saturation and Displacement Mechanism. *Environmental Science & Technology*, *49*(1), 537-543. (PMID: 25427299) doi: 10.1021/es504510y

Yortsos, Y. C., Xu, B., & Salin, D. (1997). Phase diagram of fully developed drainage in porous media. *Phys. Rev. Lett.*, *79*, 4581–4584. doi: 10.1103/PhysRevLett.79.4581

Zacharoudiou, I., & Boek, E. S. (2016). Capillary filling and Haines jump dynamics using free energy Lattice Boltzmann simulations. *Advances in Water Resources*, *92*, 43–56.

Zacharoudiou, I., Boek, E. S., & Crawshaw, J. (2018). The impact of drainage displacement patterns and Haines jumps on CO_2 storage efficiency. *Scientific reports*, *8*(1), 15561.

Zacharoudiou, I., Chapman, E. M., Boek, E. S., & Crawshaw, J. P. (2017). Pore-

filling events in single junction micro-models with corresponding lattice Boltzmann simulations. *Journal of Fluid Mechanics*, *824*, 550-573. doi: 10.1017/jfm.2017.363

Zhang, C., Oostrom, M., Wietsma, T., Grate, J., & Warner, M. (2011). Influence of Viscous and Capillary Forces on Immiscible Fluid Displacement: Pore-Scale Experimental Study in a Water-Wet Micromodel Demonstrating Viscous and Capillary Fingering. *Energy & Fuels*, *25*(8), 3493-3505. doi: 10.1021/ef101732k

Zhao, B., MacMinn, C. W., & Juanes, R. (2016). Wettability control on multiphase flow in patterned microfluidics. *Proceedings of the National Academy of Sciences*, *113*(37), 10251-10256. doi: 10.1073/pnas.1603387113